High-Precision Sub-Nyquist Sampling System Based on Modulated Wideband Converter for Communication Device Testing

Zolboo Byambadorj, *Graduate Student Member, IEEE*, Koji Asami, *Member, IEEE*, Takahiro J. Yamaguchi, *Member, IEEE*, Akio Higo, *Member, IEEE*, Masahiro Fujita, *Member, IEEE*, and Tetsuya Iizuka, *Senior Member, IEEE*

***Abstract*— This paper proposes a new method of constructing a compensation filter for the modulated wideband converter (MWC) system. The proposed method can be directly used in the MWC circuit without disconnecting any components. Furthermore, the non-ideal transfer characteristics of the real mixer output and the real ADC input are taken into account in the proposed compensation filter. The proposed method can be utilized in the advanced MWC that enables more flexibility in the design parameters of the MWC. This paper also demonstrates the reconstruction of the Bluetooth signal as a practical example for the evaluation of the reconstruction performance. The MWC successfully reconstructs the time-domain waveform of the signal based on the proposed compensation filter. Even in the case that the total effective number of channels in MWC is small as close to the necessary condition of the MWC, the error vector magnitude (EVM) was still under 1%, which is acceptable for Bluetooth device testing applications.**

***Index Terms*— Bluetooth signal, modulated wideband converter, compressed sensing, sparse wideband signal spectrum sensing, time-domain waveform reconstruction, practical implementation, compensation filter.**

I. Introduction

EVERY human-made RF signals are often sparse in the allocated band. For example, in the wireless standard IEEE-802.11, allocated wideband signal is centered at the 2.4 GHz with several numbers of active bands depending on the surrounding users. To capture such signal, it is common to sample the signal over the full band of interest with Nyquist rate after the downconversion and the low-pass filter. To reduce the burden of the sampling, a sub-Nyquist sampling system named modulated wideband converter (MWC) that uses reduced sampling rate in multi-band settings below Nyquist rate has been widely studied [1]–[11].

MWC and other compressed sensing architectures are notable candidates for some specific applications where a wideband sparse signal is used, including cognitive radio [12]–[14], spectrum analyzer [15], [16], radar [17], [18], total harmonic distortion testing [19]–[22] and ultrasound imaging [23], [24]. However, the possibility of the MWC are not limited to these applications. Wireless device testing in automatic test equipment (ATE) is another candidate. For example, Bluetooth signal uses frequency hopping technique that pseudo-randomly switches the carrier frequency in each time slot. Although the carrier frequency is unknown in advance especially from the testing side, this random property can be advantageously handled in the MWC framework. To demodulate the Bluetooth signal, it is necessary to reconstruct the time-domain waveform.

To the best of our knowledge, the first practical challenge to apply the MWC to the communication device testing is a degradation on noise performance in the MWC reconstruction. In [4]–[6], the noise figure (NF) analysis of the system was made only at the output of the ADC. To use the MWC in a practical RF receiver, it is necessary to estimate the NF of MWC to optimize the sensitivity of the receiver. The NF of the MWC including the contribution of its matrix operation is analytically investigated in [25], [26].

The recovery process and the reconstruction procedure for the sensed multiband sparse signal is ideally well-defined by sensing matrix of the compressed sensing in mathematical frameworks. However, the existing implementations [4]–[6], [10], [27]–[32] including quadrature analog-to-information converter (QAIC) [33], [34], time-segmented QAIC (TS-QAIC) [35] and random triggering based modulated wideband compressive sampling (RT-MWCS) [36] face several practical issues related to the non-ideality of the analog components including mixer, low-pass filter (LPF) and analog-to-digital converter (ADC) that cause uncertain deviation on the sensing matrix from its ideal value. Without calibrating the sensing matrix, realization of the reconstruction and the recovery of support becomes infeasible. The works [10], [27]–[29], [37]–[39] exploit the estimation method for actual sensing matrix based on a set of sequential measurements of single-tones with known frequencies. This iterative method

Manuscript received February 15, 2021; revised May 3, 2021; accepted May 19, 2021. Date of publication June 7, 2021; date of current version January 10, 2022. This article was recommended by Associate Editor M. Mozaffari Kermani. *(Corresponding author: Zolboo Byambadorj.)*

Zolboo Byambadorj is with the Department of Electrical Engineering and Information Systems, The University of Tokyo, Tokyo 113-0032, Japan (e-mail: zolboo@silicon.u-tokyo.ac.jp).

Koji Asami is with Advantest Laboratories Ltd., Miyagi 989-3124, Japan (e-mail: koji.asami@advantest.com).

Takahiro J. Yamaguchi, Akio Higo, Masahiro Fujita, and Tetsuya Iizuka are with the VLSI Design and Education Center, The University of Tokyo, Tokyo 113-0032, Japan (e-mail: takahiro.j.yamaguchi@vdec.u-tokyo.ac.jp; higo@if.t.u-tokyo.ac.jp; fujita@ee.t.u-tokyo.ac.jp; iizuka@vdec.u-tokyo.ac.jp).

Color versions of one or more figures in this article are available at https://doi.org/10.1109/TCSI.2021.3084684.

Digital Object Identifier 10.1109/TCSI.2021.3084684

is extremely time-consuming and the digital processing of the calibration turns into computationally complex due to the large number of calibration signals for real-time applications. In addition, the accuracy of the calibration may be deteriorated by the measurement-to-measurement timing mismatch. We have proposed a new calibration method that estimates the actual sensing matrix coefficients of the MWC only with a single measurement based on a pilot multi-tone signal [40]. Not only the number of measurements is reduced in this method, but also the impact of the measurement-to-measurement timing fluctuations on the calibrated sensing matrix is fundamentally removed.

However, there is another factor that also limits the reconstruction performance of the MWC. It has been reported that the impact of the non-ideal LPF critically degrades the MWC reconstruction performance [41]–[43]. One of the excellent ways to build the compensation filter is to use the least-squares method for finding the optimal coefficients of the compensation filter [44]–[46]. However, it is applicable only to basic MWC ($q = 1$), which makes the method not a good candidate in practical implementations. This method also needs many measurements, which takes a long time to build the compensation filter. Another method that is usable for the advanced MWC ($q > 1$) is proposed in [47], [48]. However, these previous works have some drawbacks. First, it was impossible to estimate the transfer characteristics of the LPF without disconnecting the LPF circuit from the MWC system, making the method infeasible in some practical implementations. Second, the compensation filter cannot compensate for the non-ideality of the mixer output and the ADC input characteristics.

This paper proposes a new method to construct the compensation filter that can be directly used in the MWC system without disconnecting any components. Thus, the non-ideal characteristics of the mixer output and the ADC input are taken into account together with that of the LPF in the proposed compensation filter. The proposed method can be utilized in the advanced MWC that enables more flexibility in the design parameters of the MWC. The proposed advanced digital compensation filter relaxes the analog filter requirement in the practical implementation of the MWC. Besides above advantages, the proposed method can also obtain the necessary measurement for the compensation filter in a single measurement while the previous methods require many measurements. While all the previous results are based on simulation due to the infeasibilities for the practical measurement setup [41]–[48], in this paper we will demonstrated the performance of the proposed method with the actual measurement results using the on-board implementation of the MWC system.

This paper uses Bluetooth signal as a practical example for the evaluation of the reconstruction performance. The MWC successfully reconstructs the time-domain waveform of the signal based on the proposed compensation filter. The measured EVM of the reconstructed waveform is under 1%, which is totally acceptable for Bluetooth device testing applications. The application of the MWC to the reconstruction of the real modulated signal has not been demonstrated in any prior works. However, in this paper, we explore a possibility of the MWC for capturing those real modulated signals to prove its feasibility in this area.

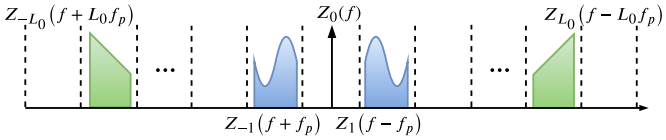

Fig. 1. Conceptual spectrum of the input sparse signal. The number of slots within the band of interest is counted as L_0.

II. Preliminaries

This section briefly explains the mathematical backgrounds of the MWC. Table I defines some key parameters of the MWC. Frequency domain representation is useful to define a wideband sparse signal [25]. The frequency-domain representation of a multiband signal can be modeled as

$$X(f) = \sum_{l \in \mathbf{S}} Z_l(f - lf_p), \tag{1}$$

where $Z_l(f)$ is a separate spectrum slice placed at baseband, and carrier frequencies are assumed to be aligned with integer multiples of f_p here. $\mathbf{S}$ is a support of $X(f)$, which is a set of N indices that correspond to carrier frequencies (including conjugate frequencies) of active bands. As shown in Fig. 1, the frequency-shifted version of $Z_l(f)$ is sparsely placed in the frequency domain. The number of slots within the band of interest is counted as L. As the signal is spectrally sparse, $N \ll L$.

A. MWC

Based on the MWC settings defined in [2], a basic MWC system is illustrated in Fig. 2 [25]. The design parameter notations are summarized in Table I. A periodic sign function (PSF) $p_i(t)$ is a periodically constant sequence with M length that switches the level between -1 and $+1$ for $T_p = 1/f_p$ interval [2]. A frequency-domain illustration of a PSF $p_i(t)$ that is decomposed into Fourier series coefficients $c_{i,l}$ located at lf_p is shown in Fig. 3(a). These components downconvert corresponding bands or spectrum slices of the input signal with individual amplitudes as in Fig. 3(b), where the digital output signal $y_i[n]$ in i-th channel through Fourier transform can be expressed as

$$Y_i(e^{j\omega T_s}) = \sum_{l=-L_0}^{L_0} c_{i,-l} Z_l(f). \tag{2}$$

Here, Y_i is a frequency-domain representation of $y_i[n]$. If (2) is written as a vector signal $\mathbf{Y} = [Y_1(e^{j\omega T_s}), Y_2(e^{j\omega T_s}), \ldots Y_m(e^{j\omega T_s})]^T$ in matrix form where the superscript T represents transpose, the generalized form is given by

$$\mathbf{Y} = \mathbf{AZ}, \tag{3}$$

where $\mathbf{Z}$ points out separate spectrum slices of the input discrete-time signal and $\mathbf{A}$ is a sensing matrix that is defined

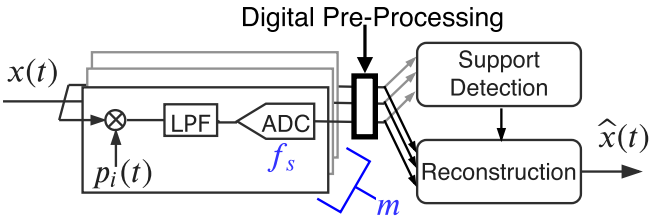

Fig. 2. A basic MWC system block diagram in general. The wideband sparse signal $x(t)$ is injected to the RF input path of the mixer. The LO input path is provided with a periodic sign function $p_i(t)$. The digital pre-processing part includes our proposed compensation filter.

TABLE I
MWC DESIGN PARAMETERS

Design Parameters	Notation
Periodic Sign Function (PSF) frequency	f_p
Number of active bands	N
Number of slots in band of interest	L
Band of interest	$W = Lf_p$
Number of symbols in PSF	M
Number of channels	m
Number of digital channels in a single channel	q
Sampling rate of ADC	$f_s = qf_p$

only by Fourier series coefficients of all the PSF signals as

$$[\mathbf{A}]_{i,j} = c_{i,j}, \quad i \in [1, m], \quad j \in [-L_0, L_0]. \tag{4}$$

The parameter q in Table I enables design flexibility between the number of analog channels and the complexity of digital signal processing by increasing the sampling rate of the ADC in each channel to capture more frequency bands into digital domain. Although the detailed explanation is omitted in this paper, in the case of a so-called advanced MWC, q (> 1) digital channels are effectively extracted from a single analog channel [25]. After capturing the digital vector signal $\mathbf{Y}$, the support frequencies of active bands in the input sparse signal can be recovered by Greedy algorithms such as matching pursuit (MP), orthogonal matching pursuit (OMP), etc [49]. Recovered support frequency indicates nonzero signal indices of $\mathbf{Z} = [Z_{-L_0}(f), \ldots, Z_0(f), \ldots, Z_{L_0}(f)]^T$. These nonzero signals can be reconstructed using least-squares through the multiplication of the pseudo-inverse matrix as follows:

$$\hat{\mathbf{Z}}_S = \mathbf{A}_\mathbf{S}^\dagger \mathbf{Y} \tag{5}$$

Here, subscript $\mathbf{S}$ denotes a set of row indices where $\mathbf{Z}$ takes nonzero values.

To achieve proper reconstruction, the MWC system has to meet the *necessary condition*. Theoretically, the necessary condition for exact recovery of $\mathbf{S}$ is defined as follows: a number of channels m is needed to be $m \geq 2N$ for blind detection of arbitrary support frequencies of the input wideband sparse signal [2]. However, if the support is correctly found, $m \geq N$ is sufficient for the perfect reconstruction of the input signal.

B. Calibration of the Sensing Matrix

In the practical implementation, the sensing matrix $\mathbf{A}$ in (3) is deteriorated by the non-ideality of the real circuits that severely impacts the reconstruction performance. There are numerous calibration techniques for the sensing matrix [10], [27]–[29], [37]–[40]. Among them, we exploit the simultaneous estimation technique of the sensing matrix [40]. To use the calibration, the input signal should be specific multi-tones that are written as

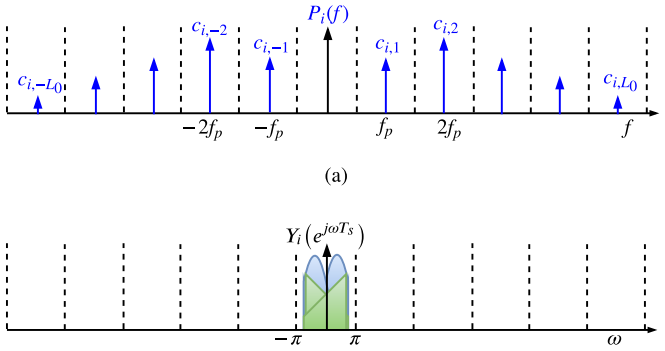

Fig. 3. (a) Fourier Series of the PSF for i-th channel and (b) DTFT of the sampled signal in i-th channel of the basic MWC.

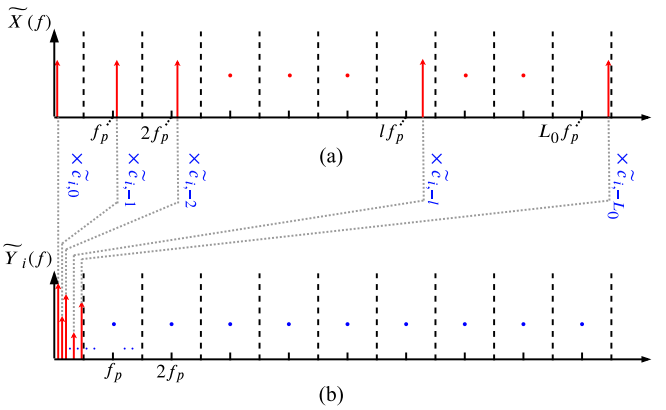

Fig. 4. (a) The frequency-domain representation $\tilde{X}(f)$ of the calibration signal $\tilde{x}(t)$ and (b) i-th output of the ADC.

$$\tilde{x}(t) = \sum_{l=1}^{L_0} \cos(2\pi(lf_p + f_l)t + \phi_l), \tag{6}$$

where ϕ_l is an initial phase and f_l is a pilot single-tone frequency that lies within $f_p/2$. The frequency-domain representation of $\tilde{x}(t)$ is illustrated in Fig. 4(a). The set of the phases is important to limit the crest factor in order to maximize the dynamic range within a limited full-scale range of the ADC. For this purpose, the Newman phases are used to present low crest factor [50].

Then with this $\tilde{x}(t)$ as an input, the discrete-time Fourier transform of the i-th output (2) of the ADC is given by

$$\tilde{Y}_i(e^{j\omega T_s}) = \sum_{l=-L_0}^{L_0} \tilde{c}_{i,-l}\delta(f - f_l). \tag{7}$$

Here, $\tilde{c}_{i,-l}$ is a Fourier series coefficients of the *actual* PSF, which is not equal to the *ideal* $c_{i,-l}$. Each single tone at f_l of the pilot signal is mixed with the corresponding *actual* coefficient $\tilde{c}_{i,-l}$ of the PSF in Fig. 3(a). The downconverted part of the mixer output is illustrated in Fig. 4(b). The main advantage of the pilot signal can be seen in (7) as well as

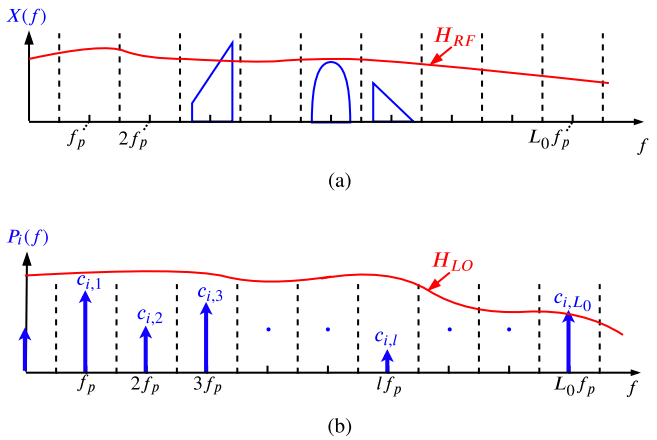

Fig. 5. (a) The frequency response non-ideality on RF path, and (b) the frequency response non-ideality on LO path diagram.

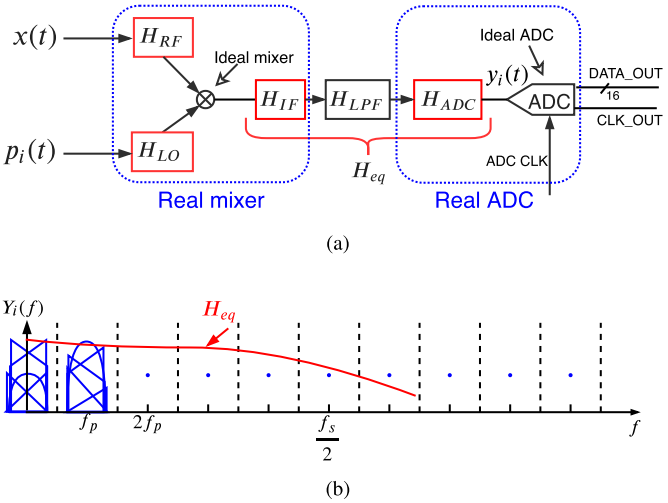

Fig. 6. (a) The conceptual non-idealities of the MWC, and (b) the equivalent frequency response of all non-linearities.

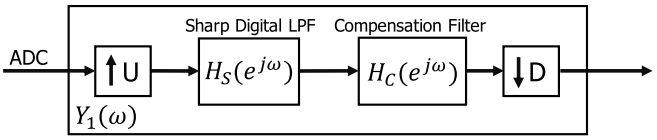

Fig. 7. The block diagram of digital pre-processing.

in Fig. 4(b); the downconverted components are disjoint in the frequency-domain.

In the frequency-domain of the mixer output, the actual coefficients of the sensing matrix can be independently calculated as

$$\tilde{c}_{i,l} = \frac{\tilde{Y}_i(e^{j2\pi(f_l)T_s})}{\tilde{Z}_l(f_l)} \quad \text{for all} \quad l \in [-L_0, L_0],\ i \in [1, m]. \tag{8}$$

The calculation of the whole sensing matrix coefficients needs only a single measurement with the pilot signal in the proposed calibration method [40]. This calibration method is exploited in the actual measurements in this paper.

III. Advanced Digital Compensation Filter Design for Digital Pre-Processing of MWC

The ideal LPF has constant amplitude and linear phase characteristics on the passband, while zero amplitude entirely over the stopband. Every practical LPF can not achieve such ideal characteristics. The non-ideal LPF in the MWC introduces several unwanted impacts on the mixed signal. Firstly, the passband may have non-constant amplitude characteristics. Secondly, the phase does not change linearly to the frequency. The third is that the stopband does not entirely reject the signal beyond cut-off frequency. In the MWC, those remained signals severely interfere with the reconstruction performance. So it is recommended to perform an oversampling in the ADC to apply a sharp digital filter in the digital domain. In this way, the requirement for the non-ideal LPF is relaxed. However, the non-ideal characteristics in the passband still need to be equalized with a compensation filter.

A. Non-Ideal Frequency Characteristic Model of the MWC

In the practical implementation of the MWC, the input signal path has non-ideal frequency response H_{RF} due to the input parasitic impedance of the mixer as shown in Fig. 5(a). Similarly, the LO path has its own non-ideal frequency response H_{LO} as illustrated in Fig. 5(b). The impact of LO path non-ideality is considered as follows. The Fourier series coefficients of the i-th PSF becomes

$$\tilde{c}_{i,l} = c_{i,l} H_{LO}(lfp), \tag{9}$$

where the $\tilde{c}_{i,l}$ is the actual coefficient while $c_{i,l}$ is the ideal coefficient as introduced in Sect. II-A. This paper aims to generalize the compensation filter for equalizing all the frequency response non-idealities including the non-ideal effect of real mixer output H_{IF} as well as the analog filter H_{LPF} and the ADC characteristics H_{ADC} as illustrated in Fig. 6(a). These non-idealities will be considered as an equivalent frequency response H_{eq} as depicted in Fig. 6(b).

$$H_{eq} = H_{IF} H_{LPF} H_{ADC} \tag{10}$$

Thus, the ADC output on i-th channel of the basic MWC (2) can be rewritten as

$$\tilde{Y}_i(e^{j\omega T_s}) = \left(\sum_{l=-L_0}^{L_0} \tilde{c}_{i,-l} Z_l(f) R_l(f) \right) H_{eq}(f), \tag{11}$$

where $R_l(f)$ is a spectrum slice of $H_{RF}(f)$ that is determined by $R_l(f) = H_{RF}(f - lf_p),\ |f| < f_p/2$. Similarly, the ADC output on i-th channel of the advanced MWC can be also given by

$$\acute{Y}_i(e^{j\omega T_s}) = \Bigg(\sum_{k=-q'}^{q'} \sum_{l=-L_0-k}^{L_0-k} \tilde{c}_{i,-(l+k)} \times Z_{l+k}(f - kf_p) R_{l+k}(f - kf_p) \Bigg) H_{eq}. \tag{12}$$

H_{LO} is taken care by the sensing matrix calibration method explained in Sect. II-B. H_{RF} is not taken care by this framework because the impact is negligibly small. If the impact

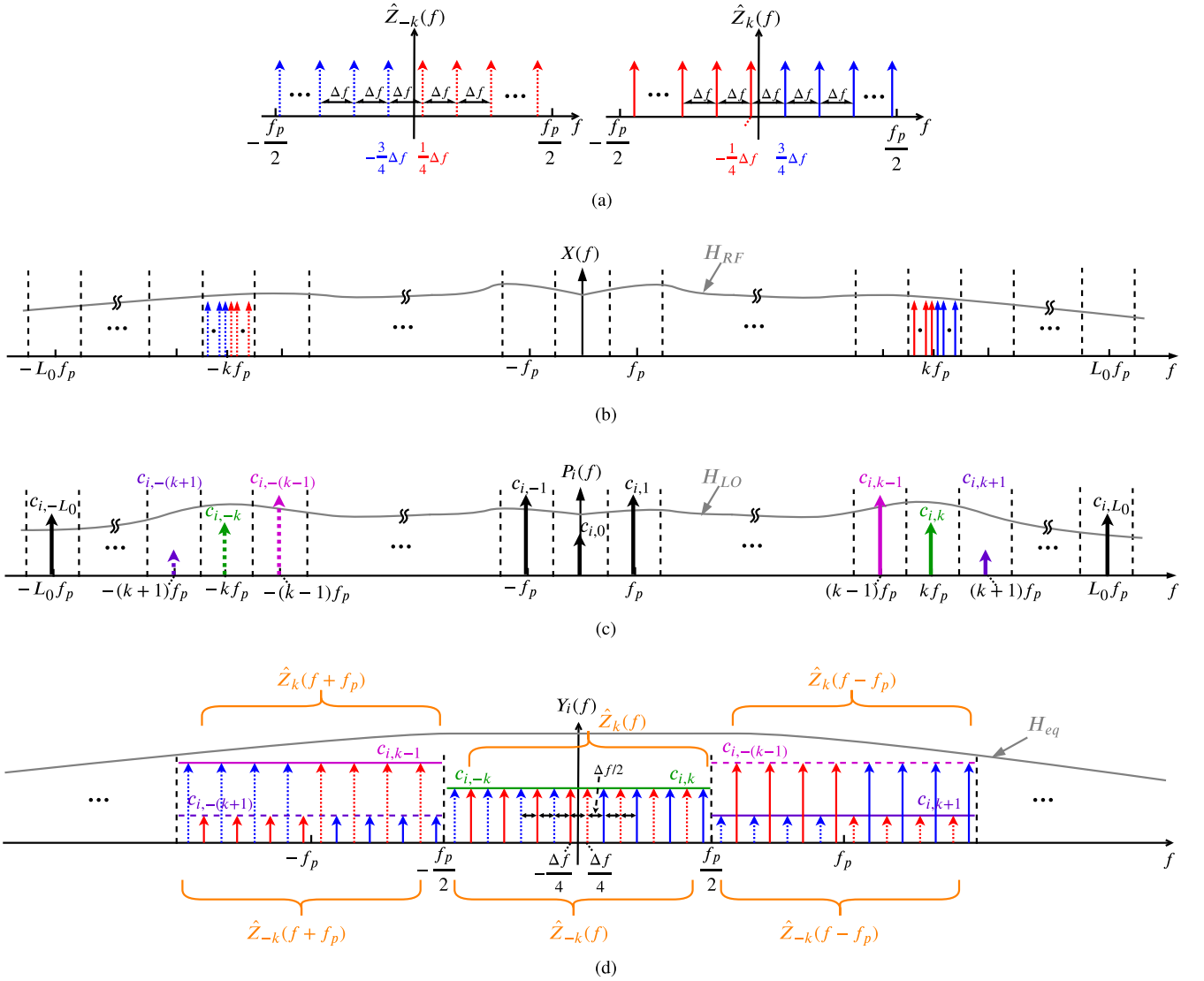

Fig. 8. (a) The conceptual baseband spectrum of the LPF training signal, (b) the original spectrum of the LPF training signal, (c) the spectrum of the i-th PSF and (d) the spectrum of the ADC input signal.

of H_{RF} becomes significant, it is still possible to reduce the impact by using additional measurements with specific training signals. Since the goal of our digital pre-processing block is to compensate the non-ideal impact of the H_{eq} in the digital domain, the first task is the estimation of the H_{eq}. The next section explains the proposed digital pre-processing method in detail.

B. Proposed Digital Compensation Filter

The block diagram of the proposed pre-processing is shown in Fig. 7. The ADC is always recommended to be operated at oversampled rate to avoid unwanted aliasing of LPF output's nonzero stopband. An appropriate choice of the oversampling rate depends on the cutoff characteristics of the LPF. By efficiently using upsampling rate U and downsampling rate D, the fractional resampling rate can be determined by U/D. After upsampler, the nonzero signals in stopband of the LPF can be rejected by the sharp digital LPF $H_S(e^{j\omega})$ with high roll-off rate or high order. Then the compensation filter $H_C(e^{j\omega})$ will be applied.

Our proposed method of building compensation filter is based on a training signal that will be applied to the MWC as the input signal. The training signal is defined by

$$x_{LPF}(t)=\sum_{\xi=0}^{G}\cos(2\pi(\xi\Delta f+\frac{\Delta f}{4}-\frac{f_p}{2}+f_c)t+\phi_\xi). \quad (13)$$

Here, ϕ_ξ is an initial phase, f_c is carrier frequency, G is the number of tones (odd number) and $\Delta f = f_p/G$ is the spacing of the tones. The set of the phases is important to limit the crest factor in order to maximize the dynamic range within a limited full-scale range of the ADC. Similar to the multi-tone signal for the sensing matrix calibration explained in Sect. II-B, the Newman phases are used to present low crest factor. According to [50], the Newman phases can be given by

$$\phi_\xi = \frac{\pi(\xi-1)^2}{G}. \quad (14)$$

The baseband spectrum of the training signal $x_{LPF}(t)$ is shown in Fig. 8(a). The original spectrum of the training

signal is illustrated in Fig. 8(b), while the spectrum of the i-th PSF is shown in Fig. 8(c). The increment of G decreases Δf that leads to finer frequency resolution, while SNR will be deducted because the amplitude of each tone is limited with more tones due to the fixed full-scale range.

In the MWC with the LPF training signal ($f_c = kf_p$), the output of the i-th ADC is given by

$$\tilde{Y}_i(e^{j\omega T_s}) = \sum_{l=0}^{\infty} \big(\tilde{c}_{i,-(k-l)} Z_k(f - lf_p) R_k(f) + \tilde{c}_{i,(k+l)} Z_{-k}(f - lf_p) R_k(-f)\big) H_{eq}(f), \quad (15)$$

where the conjugate image components $Z_{-k}(f)$ of original components $Z_k(f)$ do not conflict with its original frequencies as shown in Fig. 8(d). The dotted arrows are indicating the conjugate image $Z_{-k}(f)$ while the solid arrows are showing the original components $Z_k(f)$ in Fig. 8(d). By using this advantage, the sampled version of $H_{eq}(f)$ can be obtained by

$$\hat{H}_{eq}[\hat{f}] = \frac{\tilde{Y}_i(e^{j2\pi \hat{f} T_s})}{\sum_{l=0}^{\infty} \big(c_{i,-(k-l)} Z_k(\hat{f} - lf_p) + c_{i,(k+l)} Z_{-k}(\hat{f} - lf_p)\big)}, \quad (16)$$

where $\hat{f} = n\frac{\Delta f}{2}$, $n \in \mathbb{Z}$. Using a linear interpolation, the entire $H_{eq}(f)$ can be obtained from $\hat{H}_{eq}[\hat{f}]$. Then we construct the compensation filter $H_C(e^{j\omega})$ by using estimated $\hat{H}_{eq}(f)$ function as follows

$$H_C(e^{j\omega}) = \frac{1}{\hat{H}_{eq}(f) H_S(e^{j\omega})}. \quad (17)$$

C. Compensation Performance

To demonstrate the effectiveness of the compensation filter, the LPF training signal is reconstructed by the MWC with ($m = 4$, $q = 16$) in simulation. The spectrum of the reconstructed signal without the compensation filter is shown in Fig. 9(a). As highlighted in the figure, there are significant spurs in the reconstructed signal caused by conjugate images. Those conjugate images were not entirely rejected due to the non-ideality of the frequency response of the MWC. However, the spectrum of the reconstructed signal with the compensation filter no longer has such unwanted spurs as shown in Fig. 9(b). By using the compensation filter, the spurious-free dynamic range (SFDR) is increased from 45 dB to 66 dB. As long as the sensing matrix calibration and the compensation filter are exploited, the reconstruction of the input signal can be accurately done even if the signal occupies two (or more) spectrum slices, which will be demonstrated with the measurement results in Sect. IV-C.

IV. Practical Implementation and Measurement Results of MWC Reconstruction

A. Implementation Setups and MWC Design Parameters

The on-board implementation of the MWC system is shown in Fig. 10. The splitter board is designed to distribute the input signal to 4 separate single-channel MWC boards.

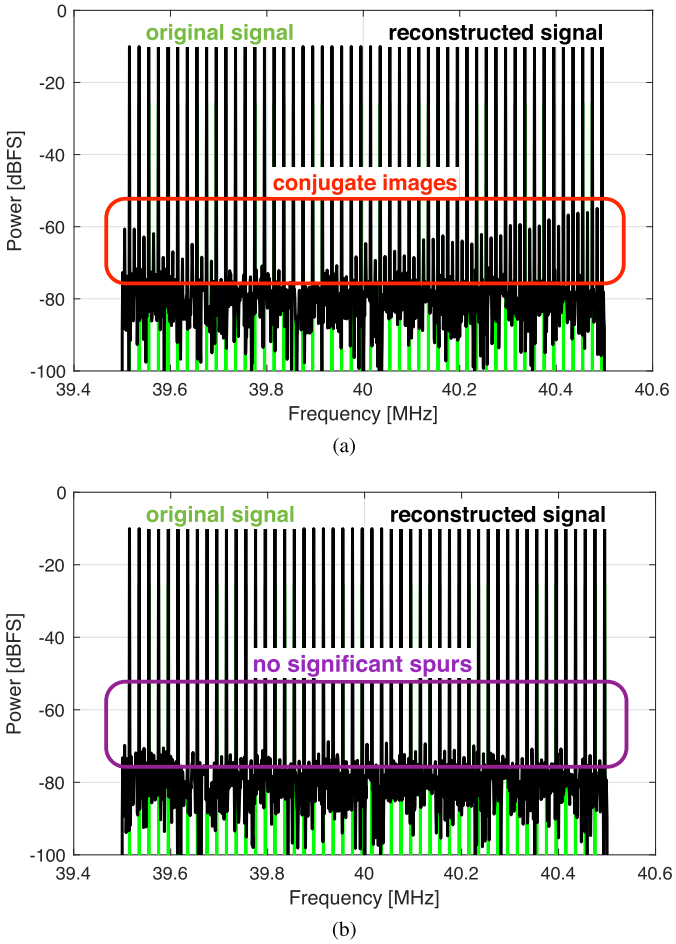

Fig. 9. (a) The reconstructed spectrum without the compensation filter and (b) The reconstructed spectrum with the compensation filter.

The single-channel MWC components excluding the active LPF in [40] are integrated onto the single board. In this paper, a passive 9-th order LC filter with $f_{\text{cut-off}} = 30$ MHz cut-off frequency is designed on the board. The design parameters of the implemented MWC are summarized in Table II. Note that N, L, M parameters count conjugate frequency components as well.

B. Construction of Compensation Filter

The actual non-ideal frequency response should be estimated to construct the proposed compensation filter. In this experiment, the LPF training signal (13) is used with $G = 50$, $f_c = 11$ MHz. The spectrum of the ADC raw input signal is shown in Fig. 11. Due to the non-ideal characteristics of the LPF, the amplitudes of the tones are not flat in each frequency band. Also, there are spurs at integer multiples of f_p (1 MHz, 2 MHz, 3 MHz, …), which is introduced by LO leakage in the analog mixer. We just ignore those spurs in the estimation of the actual LPF. The dynamic range and non-linearity of the external signal source may limit the compensation accuracy. The signal source should have better noise floor than the noise contributions of the MWC system itself or the incoming actual signal under test so that the compensation accuracy is not limited by the training signal. Also the unwanted spurs due to the non-linearity of the RF front end as well as the

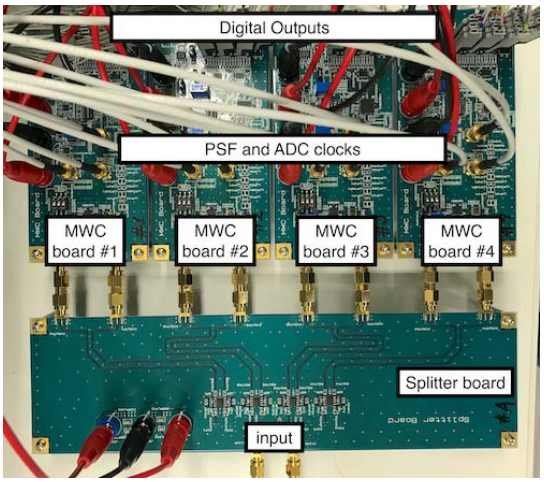

Fig. 10. The 4-channel MWC implementation boards.

TABLE II
THE DESIGN PARAMETERS OF MWC IMPLEMENTATION

Implementation Design Parameters	Notation	Value
Periodic Sign Function (PSF) frequency	f_p	1 MHz
Number of active bands	N	2
Number of slots in band of interest	L	160
Band of interest	W	160 MHz
Bandwidth of active band	B	1 MHz
Number of symbols in PSF	M	500
Number of channels	m	4
Carrier Frequencies	f_i	$(11-90)$ MHz
Number of digital channels	q	up to 17
Sampling rate of ADC	f_s	100 MHz
Number of bits on ADC	NOB	16 bits
Cut-off frequency of LPF	$f_{\text{cut-off}}$	30 MHz
Oversampling rate of ADC	$f_s/2f_{\text{cut-off}}$	$5/3$
Upsampling rate	U	3
Downsampling rate	D	10

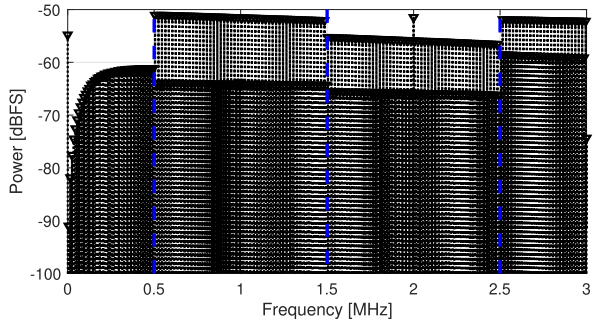

Fig. 11. The spectrum of the raw LPF training signal at the ADC output.

training signal will cause some error. Thus the external signal source that generates the training signal should have better linearity than the RF front end of the MWC system. Based on the spectrum's sampling points, the amplitude and the phase responses of the actual non-ideality are estimated as plotted with blue solid lines in Fig. 12(a) and Fig. 12(b), respectively. Based on the estimated responses, the amplitude and the phase responses of the compensation filter are built as shown with green dashed lines in Fig. 12(a) and Fig. 12(b), respectively, which almost perfectly reproduce the desired characteristics for compensation. This compensation filter is directly used to reconstruct the LPF training signal to test its performance. The result is shown in Fig. 13. The non-flat shape of the LPF training signal within each frequency band in Fig. 11 is fixed

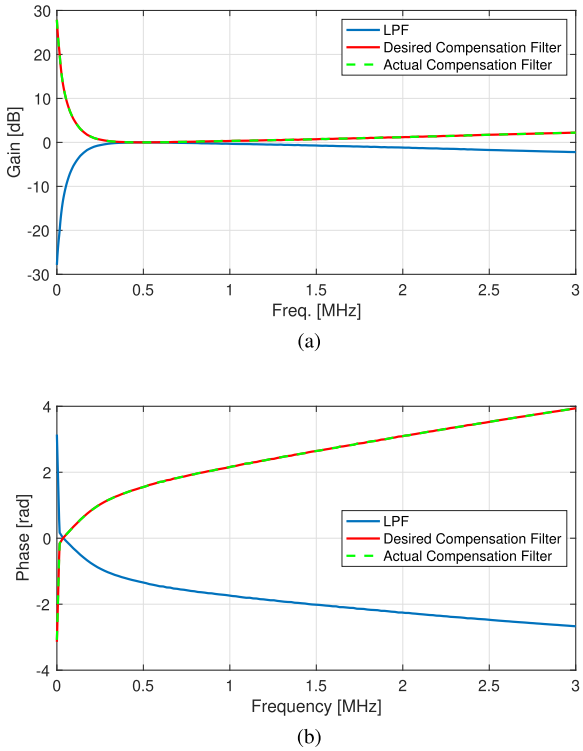

Fig. 12. (a) The amplitude response of the compensation filter and (b) the phase response of the compensation filter.

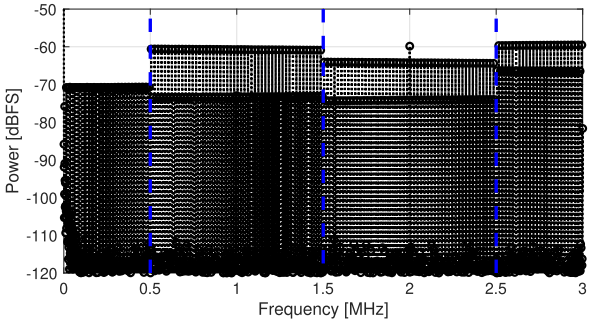

Fig. 13. The spectrum of the training signal after applying the compensation filter.

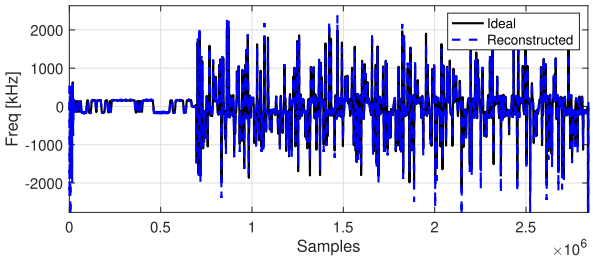

Fig. 14. The instantaneous frequency of the reconstructed Bluetooth signal with 2 MHz bandwidth ($m = 4,\ q = 16$).

to have flat shape after the compensation filter as shown in Fig. 13.

C. Measurement of Bluetooth Signal

We exploit the proposed MWC-based high-precision sub-Nyquist sampling system for the measurement of Bluetooth signal. The Bluetooth enhanced data rate (EDR) signal is generated by the commercially available software. The packet type

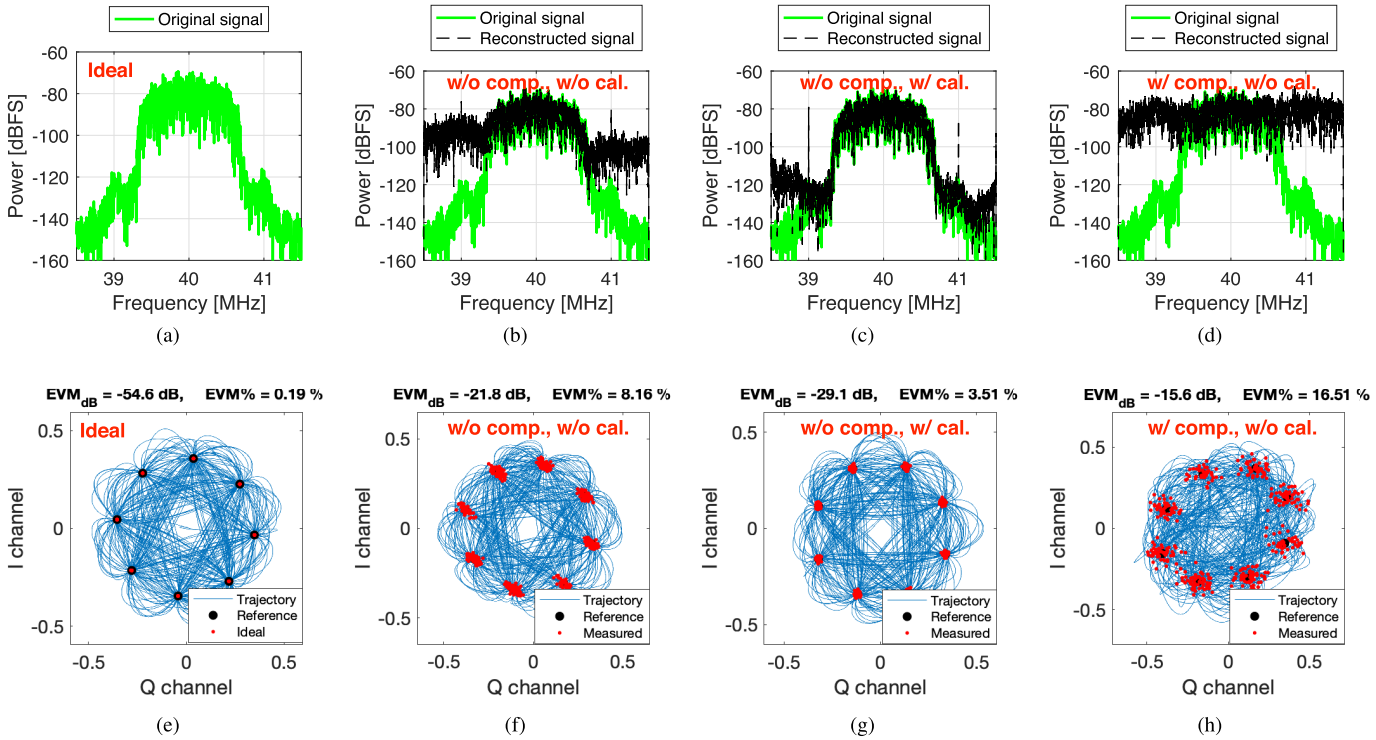

Fig. 15. Frequency-domain spectrum of (a) the input Bluetooth signal modulated at 40 MHz, (b) the reconstructed Bluetooth signal without the compensation filter (w/o comp.) and without the sensing matrix calibration (w/o cal.), (c) that without the compensation filter (w/o comp.) and with the sensing matrix calibration (w/ cal.) and (d) that with the compensation filter (w comp.) and without the sensing matrix calibration (w/o cal.). The constellation diagram of (e) the demodulated ideal input Bluetooth signal, (f) the reconstructed Bluetooth signal without the compensation filter (w/o comp.) and without the sensing matrix calibration (w/o cal.), (g) that without the compensation filter (w/o comp.) and with the sensing matrix calibration (w/ cal.) and (h) that with the compensation filter (w/ comp.) and without the sensing matrix calibration (w/o cal).

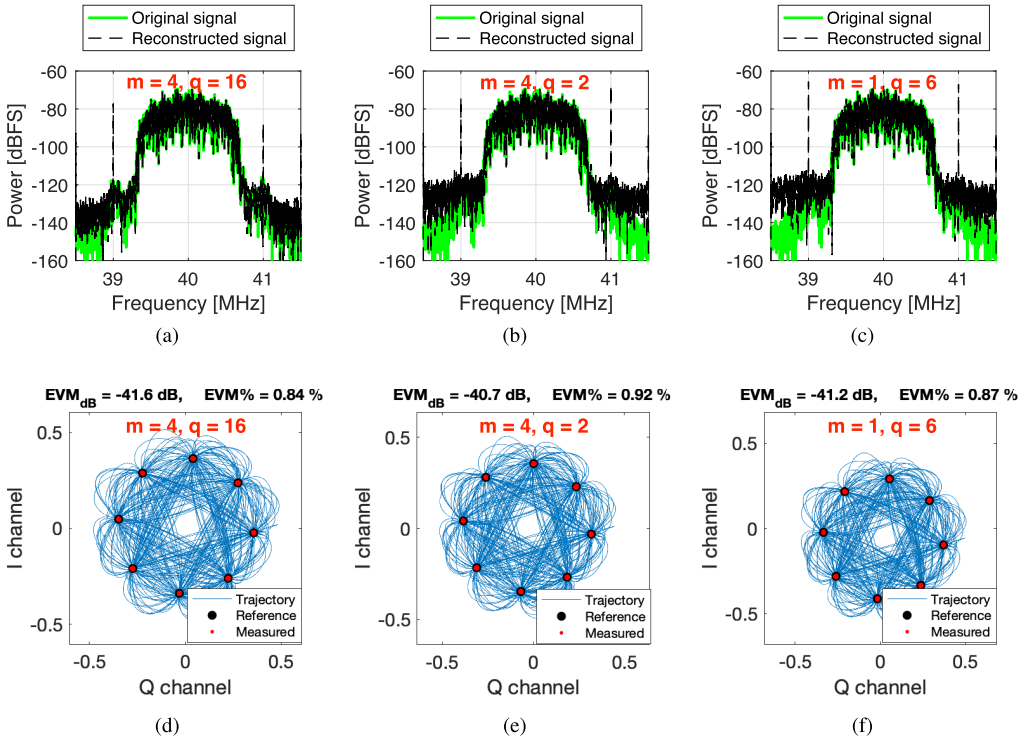

Fig. 16. Frequency-domain spectrum of (a) the reconstructed Bluetooth signal with the compensation filter (w/ comp.) and with the sensing matrix calibration (w/ cal.) by the MWC with $m = 4$, $q = 16$, (b) that reconstructed with $m = 4$, $q = 2$ and (c) that reconstructed with $m = 1$, $q = 6$. The constellation diagram of (d) the reconstructed Bluetooth signal with the compensation filter (w/ comp.) and with the sensing matrix calibration (w/ cal.) by the MWC with $m = 4$, $q = 16$, (b) that reconstructed with $m = 4$, $q = 2$ and (c) that reconstructed with $m = 1$, $q = 6$.

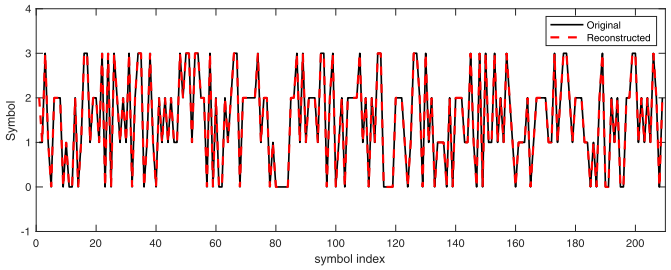

Fig. 17. The demodulated symbols of the reconstructed Bluetooth signal with 2 MHz bandwidth ($m = 4,\ q = 16$).

is set to 2-DH5 that uses 4-DPSK modulation for the payload. The Bluetooth signal is generated at 40 MHz carrier frequency. Along with the main spectrum slice of the Bluetooth signal, two neighboring sidebands are reconstructed in the MWC to achieve the EVM below 1%. To demodulate the Bluetooth signal, first, the frequency demodulation should be performed to the reconstructed signal. The instantaneous frequency is shown in Fig. 14. The GFSK modulated digital sequence can be seen in this figure. The ideal spectrum and the constellation diagram of the Bluetooth signal are shown in Fig. 15(a) and Fig. 15(e), respectively. The reconstructed spectrum and the constellation diagram based on the MWC without both of the compensation filter and the calibrated sensing matrix ($m = 4,\ q = 16$) are shown in Fig. 15(b) and Fig. 15(f), respectively. The EVM is 8% which is not acceptable for testing purpose. Similarly, without the compensation filter but with the calibrated sensing matrix case is shown in Fig. 15(c) and Fig. 15(g). The case with the compensation filter but without the calibrated sensing matrix is shown in Fig. 15(d) and Fig. 15(h). In terms of EVM and the similarity between the reconstructed spectrum and the original spectrum, these cases do not have sufficient performance, either. However, in the case with both the compensation filter and the calibrated sensing matrix, the performance is noticeably improved as shown in Fig. 16(a) and Fig. 16(d). Even in the reduced MWC ($m = 4,\ q = 2$) case in Fig. 16(b) and Fig. 16(e), the EVM performance is below 1%, which is still in the acceptable range for Bluetooth device testing. In the case of single-channel MWC ($m = 1,\ q = 6$), the reconstructed spectrum and the constellation are shown in Fig. 16(c) and Fig. 16(f), respectively. Also, the EVM performance is still lies in the acceptable range, even though the side-band part of the reconstructed spectrum is deteriorated. Finally, the 4-DPSK demodulated symbols are shown in Fig. 17. In the reconstructed spectra, there are two spurs at 39 MHz and 41 MHz that are caused by the LO leakage of the mixer. In the 4-DPSK demodulation, however, these spurs do not affect the EVM performance, because the 4-DPSK Bluetooth signal needs only 2 MHz bandwidth to achieve the maximum EVM performance. These results clearly demonstrate the capability of the MWC with the proposed compensation filter for the application of the communication device testing.

V. Conclusion

The digital pre-processing block is one of the essential computations in the practical implementation of the MWC. Without the compensation filter, the reconstruction performance of the MWC is not satisfactory. The proposed filter construction method can be directly used in the MWC circuit without disconnecting any components. The compensation filter can also equalize the impact of the mixer IF output, the analog filter, and the ADC input.

In the test of practical signal, we used the Bluetooth signal as an example to demonstrate the feasibility of the MWC. The MWC successfully reconstructs the time-domain waveform of the signal based on the proposed calibration techniques. Even in the case that the total effective number of channels mq is small as close to the necessary condition, the EVM was still under 1%, which is acceptable in Bluetooth device testing applications.

Further development of the proposed method can be made in several ways to improve the accuracy. First, the impact of H_{RF} may be dominant depending on the RF front-end. Using additional measurements, it is possible to compensate the impact of H_{RF} by applying individual filters with each reconstructed spectrum slices. Second, also depending on the RF front end configurations, the impact of its non-linearity may limit the performance of the MWC. We are trying to develop a new calibration method to accurately reconstruct the wideband sparse signals even with RF front end non-linearity.

References

[1] M. Mishali and Y. C. Eldar, "Sub-Nyquist sampling," *IEEE Signal Process. Mag.*, vol. 28, no. 6, pp. 98–124, Nov. 2011.
[2] M. Mishali and Y. C. Eldar, "From theory to practice: Sub-Nyquist sampling of sparse wideband analog signals," *IEEE J. Sel. Topics Signal Process.*, vol. 4, no. 2, pp. 375–391, Apr. 2010.
[3] M. Mishali and Y. C. Eldar, "Blind multiband signal reconstruction: Compressed sensing for analog signals," *IEEE Trans. Signal Process.*, vol. 57, no. 3, pp. 993–1009, Mar. 2009.
[4] M. Mishali, Y. C. Eldar, O. Dounaevsky, and E. Shoshan, "Xampling: Analog to digital at sub-Nyquist rates," *IET Circuits, Devices Syst.*, vol. 5, no. 1, pp. 8–20, Jan. 2011.
[5] D. Adams, Y. Eldar, and B. Murmann, "A mixer frontend for a four-channel modulated wideband converter with 62 dB blocker rejection," in *Proc. IEEE Radio Freq. Integr. Circuits Symp. (RFIC)*, May 2016, pp. 286–289.
[6] D. Adams, Y. C. Eldar, and B. Murmann, "A mixer front end for a four-channel modulated wideband converter with 62-dB blocker rejection," *IEEE J. Solid-State Circuits*, vol. 52, no. 5, pp. 1286–1294, May 2017.
[7] T. Chen, L. Liu, and Z. Zhao, "Compressed sampling signal detection method based on modulated wideband converter," in *Proc. IEEE Adv. Inf. Manage., Communicates, Electron. Autom. Control Conf. (IMCEC)*, Oct. 2016, pp. 223–227.
[8] M. A. Lexa, M. E. Davies, and J. S. Thompson, "Reconciling compressive sampling systems for spectrally sparse continuous-time signals," *IEEE Trans. Signal Process.*, vol. 60, no. 1, pp. 155–171, Jan. 2012.
[9] E. Matusiak and Y. C. Eldar, "Sub-Nyquist sampling of short pulses," *IEEE Trans. Signal Process.*, vol. 60, no. 3, pp. 1134–1148, Mar. 2012.
[10] P. Wang, F. You, and S. He, "An improved signal reconstruction of modulated wideband converter using a sensing matrix built upon synchronized modulated signals," *Circuits, Syst., Signal Process.*, vol. 38, no. 7, pp. 3187–3210, Jul. 2019, doi: 10.1007/s00034-018-1009-z.
[11] Y. Zhao, Y. H. Hu, and J. Liu, "Random triggering-based sub-Nyquist sampling system for sparse multiband signal," *IEEE Trans. Instrum. Meas.*, vol. 66, no. 7, pp. 1789–1797, Jul. 2017.
[12] J. Mitola, "Software radios—Survey, critical evaluation and future directions," in *Proc. Nat. Telesyst. Conf. (NTC)*, May 1992, pp. 13–15.
[13] S. Haykin, "Cognitive radio: Brain-empowered wireless communications," *IEEE J. Sel. Areas Commun.*, vol. 23, no. 2, pp. 201–220, Feb. 2005.
[14] K. Entesari and P. Sepidband, "Spectrum sensing: Analog (or partially analog) CMOS real-time spectrum sensing techniques," *IEEE Microw. Mag.*, vol. 20, no. 6, pp. 51–73, Jun. 2019.

[15] C. Tao, L. Lizhi, G. Muran, and Y. Zhigang, "Frequency spectrum analysis of compressed sampling datum based on modulated wideband converter," in *Proc. IEEE Inf. Technol., Netw., Electron. Autom. Control Conf.*, May 2016, pp. 996–1000.
[16] Q. Li, Z. Li, and J. Li, "Wideband spectrum sensing based on modulated wideband converter with nested array," *IET Commun.*, vol. 15, no. 2, pp. 224–231, Jan. 2021. [Online]. Available: https://ietresearch.onlinelibrary.wiley.com/doi/abs/10.1049/cmu2.12048
[17] E. Ramezani, M. F. Sabahi, and S. M. Saberali, "Space-borne compressed sensing based receiver for accurate localization of ground-based radars," *Prog. Electromagn. Res. C*, vol. 99, pp. 251–267, 2020.
[18] J. Yoo, S. Becker, M. Loh, M. Monge, E. Candes, and A. Emami-Neyestanak, "A 100MHz–2GHz 12.5× sub-Nyquist rate receiver in 90nm CMOS," in *Proc. IEEE Radio Freq. Integr. Circuits Symp.*, Jun. 2012, pp. 31–34.
[19] F. Bonavolontà, M. D'Apuzzo, A. Liccardo, and G. Miele, "Harmonic and interharmonic measurements through a compressed sampling approach," *Measurement*, vol. 77, pp. 1–15, Jan. 2016. [Online]. Available: https://www.sciencedirect.com/science/article/pii/S0263224115004352
[20] B. Palczynska, R. Masnicki, and J. Mindykowski, "Compressive sensing approach to harmonics detection in the ship electrical network," *Sensors*, vol. 20, no. 9, p. 2744, May 2020.
[21] D. Carta, C. Muscas, P. A. Pegoraro, A. Vincenzo Solinas, and S. Sulis, "Impact of measurement uncertainties on compressive sensing-based harmonic source estimation algorithms," in *Proc. IEEE Int. Instrum. Meas. Technol. Conf. (I2MTC)*, May 2020, pp. 1–6.
[22] D. Carta, C. Muscas, P. A. Pegoraro, A. V. Solinas, and S. Sulis, "Compressive sensing-based harmonic sources identification in smart grids," *IEEE Trans. Instrum. Meas.*, vol. 70, pp. 1–10, 2021.
[23] Z. Pei and Y. Wang, "Multichannel sub-Nyquist sampling for ultrasound imaging applications," in *Proc. IEEE 4th Inf. Technol. Mechatronics Eng. Conf. (ITOEC)*, Dec. 2018, pp. 830–834.
[24] R. Tur, Y. C. Eldar, and Z. Friedman, "Innovation rate sampling of pulse streams with application to ultrasound imaging," *IEEE Trans. Signal Process.*, vol. 59, no. 4, pp. 1827–1842, Apr. 2011.
[25] Z. Byambadorj, K. Asami, T. J. Yamaguchi, A. Higo, M. Fujita, and T. Iizuka, "Theoretical analysis of noise figure for modulated wideband converter," *IEEE Trans. Circuits Syst. I, Reg. Papers*, vol. 67, no. 1, pp. 298–308, Jan. 2020.
[26] Z. Byambadorj, K. Asami, T. J. Yamaguchi, A. Higo, M. Fujita, and T. Iizuka, "Theoretical analysis on noise performance of modulated wideband converters for analog testing," in *Proc. IEEE 29th Asian Test Symp. (ATS)*, Nov. 2020, pp. 1–6.
[27] W. Liu, Z. Huang, X. Wang, and W. Sun, "Design of a single channel modulated wideband converter for wideband spectrum sensing: Theory, architecture and hardware implementation," *Sensors*, vol. 17, no. 5, p. 1035, May 2017.
[28] E. Israeli *et al.*, "Hardware calibration of the modulated wideband converter," in *Proc. IEEE Global Commun. Conf.*, Dec. 2014, pp. 948–953.
[29] N. Fu, S. Jiang, L. Deng, and L. Qiao, "Successive-phase correction calibration method for modulated wideband converter system," *IET Signal Process.*, vol. 13, no. 6, pp. 624–632, Aug. 2019.
[30] M. Mishali and Y. Eldar, "Wideband spectrum sensing at sub-Nyquist rates [applications corner]," *IEEE Signal Process. Mag.*, vol. 28, no. 4, pp. 102–135, Jul. 2011.
[31] P. Wang, F. You, and S. He, "Design of broadband compressed sampling receiver based on concurrent alternate random sequences," *IEEE Access*, vol. 7, pp. 135525–135538, 2019.
[32] F. You, P. Shang, and P. Wang, "Design of a low-cost integrated RF front-end for a modulated-wideband-converter based receiver," in *Proc. IEEE Asia Pacific Microw. Conf. (APMC)*, Nov. 2017, pp. 1099–1102.
[33] R. T. Yazicigil, T. Haque, M. R. Whalen, J. Yuan, J. Wright, and P. R. Kinget, "Wideband rapid interferer detector exploiting compressed sampling with a quadrature analog-to-information converter," *IEEE J. Solid-State Circuits*, vol. 50, no. 12, pp. 3047–3064, Dec. 2015.
[34] T. Haque, R. T. Yazicigil, K. J.-L. Pan, J. Wright, and P. R. Kinget, "Theory and design of a quadrature analog-to-information converter for energy-efficient wideband spectrum sensing," *IEEE Trans. Circuits Syst. I, Reg. Papers*, vol. 62, no. 2, pp. 527–535, Feb. 2015.
[35] R. T. Yazicigil, T. Haque, M. Kumar, J. Yuan, J. Wright, and P. R. Kinget, "A compressed-sampling time-segmented quadrature analog-to-information converter for wideband rapid detection of up to 6 interferers with adaptive thresholding," in *Proc. IEEE Radio Freq. Integr. Circuits Symp. (RFIC)*, May 2016, pp. 282–285.
[36] Y. Zhao, Y. H. Hu, and J. Liu, "Random triggering based sub-Nyquist sampling system for sparse multiband signal," 2017, *arXiv:1703.01933*. [Online]. Available: http://arxiv.org/abs/1703.01933
[37] J. Park, J. Jang, and H. Lee, "A calibration for the modulated wideband converter using sinusoids with unknown phases," in *Proc. 9th Int. Conf. Ubiquitous Future Netw. (ICUFN)*, Jul. 2017, pp. 951–955.
[38] L. Chen, J. Jin, and Y. Gu, "A calibration system and perturbation analysis for the modulated wideband converter," in *Proc. IEEE 10th Int. Conf. SIGNAL Process.*, Oct. 2010, pp. 78–81.
[39] Y. K. Alp, A. B. Korucu, A. T. Karabacak, A. C. Gurbuz, and O. Arikan, "Online calibration of modulated wideband converter," in *Proc. 24th Signal Process. Commun. Appl. Conf. (SIU)*, May 2016, pp. 913–916.
[40] Z. Byambadorj, K. Asami, T. J. Yamaguchi, A. Higo, M. Fujita, and T. Iizuka, "A calibration technique for simultaneous estimation of actual sensing matrix coefficients on modulated wideband converters," *IEEE Trans. Circuits Syst. I, Reg. Papers*, vol. 67, no. 12, pp. 5561–5573, Dec. 2020.
[41] J. Zhang, N. Fu, W. Yu, and X. Peng, "Analysis of non-idealities of low-pass filter in random demodulator," *Proc. SPIE*, vol. 8759, Jan. 2013, Art. no. 87591Q.
[42] P. J. Pankiewicz, T. Arildsen, and T. Larsen, "Sensitivity of the random demodulation framework to filter tolerances," in *Proc. 19th Eur. Signal Process. Conf.*, Aug. 2011, pp. 534–538.
[43] S. Smaili and Y. Massoud, "Accurate and efficient modeling of random demodulation based compressive sensing systems with a general filter," in *Proc. IEEE Int. Symp. Circuits Syst. (ISCAS)*, Jun. 2014, pp. 2519–2522.
[44] Z. Yijiu, L. Ling, Z. Xiaoyan, and D. Zhijian, "Model calibration for compressive sampling system with non-ideal lowpass filter," in *Proc. 12th IEEE Int. Conf. Electron. Meas. Instrum. (ICEMI)*, Jul. 2015, pp. 808–812.
[45] Y. Zhao, H. Wang, and Z. Dai, "Model calibration of non-ideal lowpass filter in modulated wideband converter for compressive sampling," *COMPEL, Int. J. Comput. Math. Electr. Electron. Eng.*, vol. 34, no. 3, pp. 941–951, May 2015.
[46] Y. Chen, M. Mishali, Y. C. Eldar, and A. O. Hero, "Modulated wideband converter with non-ideal lowpass filters," in *Proc. IEEE Int. Conf. Acoust., Speech Signal Process.*, Mar. 2010, pp. 3630–3633.
[47] L.-L. Nguyen, R. Gautier, A. Fiche, G. Burel, and E. Radoi, "Digital compensation of lowpass filters imperfection in the modulated wideband converter compressed sensing scheme for radio frequency monitoring," *Signal Process.*, vol. 152, pp. 292–310, Nov. 2018. [Online]. Available: http://www.sciencedirect.com/science/article/pii/S0165168418302081
[48] L.-L. Nguyen, A. Fiche, R. Gautier, C. Canaff, E. Radoi, and G. Burel, "Implementation of modulated wideband converter compressed sensing scheme based on COTS lowpass filter with amplitude and phase compensation for spectrum monitoring," in *Proc. 15th IEEE Int. Conf. Adv. Video Signal Based Surveill. (AVSS)*, Nov. 2018, pp. 1–6.
[49] Y. C. Pati, R. Rezaiifar, and P. S. Krishnaprasad, "Orthogonal matching pursuit: Recursive function approximation with applications to wavelet decomposition," in *Proc. 27th Asilomar Conf. Signals, Syst. Comput.*, Nov. 1993, pp. 40–44.
[50] S. Boyd, "Multitone signals with low crest factor," *IEEE Trans. Circuits Syst.*, vol. CAS-33, no. 10, pp. 1018–1022, Oct. 1986.

Zolboo Byambadorj (Graduate Student Member, IEEE) received the B.S. and M.S. degrees in communication engineering from the National University of Mongolia, Ulaanbaatar, Mongolia, in 2008 and 2012, respectively, and the Ph.D. degree in electrical engineering from The University of Tokyo, Tokyo, Japan, in 2021.

In 2008, he joined the Department of Electrical and Communication Engineering, National University of Mongolia, as a Faculty Member. He is currently a Project Researcher with the D2T Research Division, VLSI Design and Education Center, The University of Tokyo. His research interests include wireless communication systems and sub-Nyquist sampling systems. He received the "Outstanding Ph.D. Thesis" Award for his Ph.D. degree.

Koji Asami (Member, IEEE) received the master's degree in electronic engineering and the Ph.D. degree in electronics and information engineering from Gunma University, Japan, in 1991 and 2009, respectively.

He joined Advantest Corporation at their Gunma Research and development Center in 1991, where he dedicated his time to researching signal processing techniques for mixed-signal and RF LSI test, including the digital modulation analysis. Since 2019, he has been researching measurement methodologies for wireless communication devices in Advantest Laboratories Ltd. He has also been a Visiting Professor with the Graduate School of Science and Technology, Gunma University, since 2015, and a Researcher with the Advantest D2T Research Division, VDEC, The University of Tokyo, since 2017. His research interests include signal processing algorithm for testing RF and analog devices and improving the automatic test equipment (ATE) performance.

Takahiro J. Yamaguchi (Member, IEEE) received the B.S. degree in applied physics from Fukui University, Fukui, Japan, in 1976, and the M.S. degree in physics and the Ph.D. degree in electronic engineering from Tohoku University, Sendai, Japan, in 1978 and 1999, respectively.

He joined Advantest Corporation in 1978, where he was a Research and Development Project Manager for Fourier analyzers, FFT-based servo analyzers, Michelson-type optical spectrum analyzers, and TV signal analyzers. Until 2017, he was with Advantest Laboratories Ltd., Japan. From 2009 to 2017, he was also a Researcher with the VDEC, The University of Tokyo. From 2009 to 2014, he was a Visiting Professor with Gunma University, Japan. He is currently the Project Academic Support Staff with the VDEC, The University of Tokyo. He and his group have presented 14 articles at ITC from year 2000, 11 articles at ISSCC, VLSI CIRCUITS, CICC, RFIC, A-SSCC, and ISCAS, and seven journal articles. He was a co-recipient of the DesignCon 2007 Best Paper and the Honorable Mention Award at ITC2010 for ITC2009 jitter separation article. From 2010 to 2015, he has served as a member of Technical Program Committee for the IEEE Custom Integrated Circuits Conference (CICC).

Akio Higo (Member, IEEE) received the B.E. degree from Seikei University, Tokyo, Japan, in 2002, and the M.E. and Ph.D. degrees from the Department of Electrical Engineering, The University of Tokyo, Tokyo, in 2004 and 2007, respectively.

From 2007 to 2012, he was an Assistant Professor with the Research Center for Advanced Science and Technology. From 2012 to 2016, he was an Assistant Professor with the World Premier Initiative Advanced Institute for Materials Research, Tohoku University, Sendai, Japan. Since 2017, he has been a Project Lecturer with the D2T Research Division, VLSI Design and Education Center, The University of Tokyo. His research interests include NEMS/MEMS, nanolighography for III–V materials and silicon, and silicon photonics.

Masahiro Fujita (Member, IEEE) received the Ph.D. degree in information engineering from The University of Tokyo in 1985 on his work on model checking of hardware designs by using logic programming languages.

In 1985, he joined Fujitsu as a Researcher and started to work on hardware automatic synthesis as well as formal verification methods and tools, including enhancements of BDD/SAT based techniques. From 1993 to 2000, he was the Director of Fujitsu Laboratories of America and headed a hardware formal verification group developing a formal verifier for real-life designs having more than several million gates. The developed tool has been used in production internally at Fujitsu and externally as well. Since March 2000, he has been a Professor with the VLSI Design and Education Center, The University of Tokyo. He has done innovative work in the areas of hardware verification, synthesis, testing, and software verification-mostly targeting embedded software and web-based programs. He has been involved in a Japanese governmental research project for dependable system designs and has developed a formal verifier for C programs that could be used for both hardware and embedded software designs. The tool is now under evaluation jointly with industry under governmental support. He has authored and coauthored ten books, and has more than 200 publications. He has been involved as a program and steering committee member in many prestigious conferences on CAD, VLSI designs, and software engineering. His current research interests include synthesis and verification in system on chip (SoC), hardware/software co-designs targeting embedded systems, digital/analog co-designs, and formal analysis, verification, and synthesis of web-based programs and embedded programs.

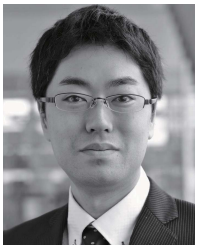

Tetsuya Iizuka (Senior Member, IEEE) received the B.S., M.S., and Ph.D. degrees in electronic engineering from The University of Tokyo, Tokyo, Japan, in 2002, 2004, and 2007, respectively.

From 2007 to 2009, he was with THine Electronics, Inc., Tokyo, as a High-Speed Serial Interface Circuit Engineer. He joined The University of Tokyo in 2009, where he is currently an Associate Professor with the Systems Design Laboratory, School of Engineering. From 2013 to 2015, he was a Visiting Scholar with the University of California, Los Angeles, Los Angeles, CA, USA. His current research interests include data conversion techniques, high-speed analog integrated circuits, digitally assisted analog circuits, and VLSI computer-aided design. He is also a member of the Institute of Electronics, Information and Communication Engineers (IEICE). He was a member of the IEEE International Solid-State Circuits Conference (ISSCC) Technical Program Committee from 2013 to 2017 and a member of the IEEE Custom Integrated Circuits Conference (CICC) Technical Program Committee from 2014 to 2019. He is also serving as a member for the IEEE Asian Solid-State Circuits Conference (A-SSCC) Technical Program Committee. He was a recipient of the Young Researchers Award from IEICE in 2002, the IEEE International Conference on Electronics, Circuits and Systems Best Student Paper Award in 2006, the Yamashita SIG Research Award from the Information Processing Society, Japan, in 2007, the 21st Marubun Research Encouragement Commendation from Marubun Research Promotion Foundation in 2018, the 13th Wakashachi Encouragement Award First Prize in 2019, and the 18th Funai Academic Prize from Funai Foundation for Information Technology in 2019. He was a co-recipient of the IEEE International Test Conference Ned Kornfield Best Paper Award in 2016. From 2016 to 2018, he has served as an Editor for *IEICE Electronics Express* (ELEX).